



# Effect of Taper Ratio at Low Reynolds Number

Lance W. Traub,\* Emilio Botero,† Rajmohan Waghela,† Ryan Callahan,† and Aaron Watson†  
Embry Riddle Aeronautical University, Prescott, Arizona 86301

DOI: 10.2514/1.C032559

A low speed wind-tunnel investigation is presented documenting the impact of taper ratio at low Reynolds number. An AR = 5.56 wing using a S8036 section was tested at  $Re = 100,000$  and  $150,000$ . Taper ratio was varied from 1 down to 0.2 in 0.2 increments. An analytic prediction method as well as extended numerical lifting line theory incorporating nonlinear section data was implemented to compare with experiment. The experimental results indicated a weak dependence of peak lift to drag ratio on taper ratio for both Reynolds numbers. Surface flow visualization showed the presence of a large laminar transitional bubble on the upper wing surface. The relative extent of the bubble was observed to increase towards the tip region for tapered planforms. Agreement between theory and experiment in terms of lift and drag estimation was good. Planform optimization using the extended numerical lifting line theory indicated that at the test conditions and using the selected airfoil section, a planform that differs from straight taper or elliptic may be most efficient.

## Nomenclature

$A$	=	constant
$A_n$	=	coefficients of Fourier series
$b$	=	wingspan
$C_D$	=	wing drag coefficient
$C_{DL}$	=	total wing drag due to lift
$C_{Dv}$	=	wing vortex drag coefficient
$C_{D_0}$	=	wing zero lift drag coefficient
$C_{D_{profile}}$	=	wing profile drag coefficient
$C_d$	=	section profile drag coefficient
$C_{dv}$	=	section vortex drag coefficient
$C_L$	=	coefficient of lift
$C_l$	=	section lift coefficient
$C_{l\alpha}$	=	sectional lift-curve slope
$\bar{c}$	=	mean geometric chord
$c$	=	airfoil chord
$c_r$	=	root chord length
$c_t$	=	tip chord length
$D$	=	drag of wing
$d$	=	sectional drag
$e$	=	planform (or Oswald) efficiency factor
$e_i$	=	inviscid planform efficiency factor
$i$	=	index
$k$	=	grouped spanwise terms
$L$	=	lift of wing
$l$	=	sectional lift
$N$	=	number of terms in Fourier series
$n$	=	index term in Fourier Series
$p$	=	exponent
$q$	=	exponent
$r$	=	spanwise division
$S$	=	wing area
$V$	=	velocity
$x$	=	chordwise coordinate
$y$	=	coordinate perpendicular to plane of symmetry
$\alpha$	=	angle of attack

$\alpha_{Cl}$	=	local angle of attack for a given sectional lift coefficient
$\alpha_{geo}$	=	geometric twist angle
$\alpha_i$	=	section induced angle of attack
$\alpha_{Stall}$	=	angle of attack of stall
$\alpha_{ZL}$	=	sectional zero lift angle of attack
$\beta$	=	exponent
$\eta$	=	normalized spanwise location, attainable leading-edge suction parameter
$\eta_m$	=	multiplier for lift and drag coefficients
$\theta$	=	angular measure
$\lambda$	=	taper ratio
$\mu$	=	dynamic viscosity
$\rho$	=	density

## Subscripts

$b$	=	back of bubble
bubble	=	streamwise length of bubble
des	=	desired
$f$	=	front of bubble
max	=	maximum
min	=	minimum
$n$	=	spanwise index
ref	=	reference
$\infty$	=	freestream

## Introduction

THE drag polar of a symmetrical wing in incompressible flight is commonly approximated as

$$C_D = C_{D_0} + C_{DL} = C_{D_0} + \frac{C_L^2}{\pi A R e} \quad (1)$$

where  $C_{D_0}$  represents the zero lift drag component and is usually associated with skin friction drag. The second term  $C_L^2/(\pi A R e)$ , is the drag due to lift and is composed of inviscid vortex drag as well as viscous sectional profile drag. In common use, the skin friction is assumed constant, while the sectional pressure drag contribution is often neglected [ $e$  then may be replaced by  $e_i$  in Eq. (1)]. The skin friction term may be estimated using experimental sectional data or a flat plate analogy.

Performance of a wing is commonly quantified in terms of its achievable  $L/D$  ratio. Examination of Eq. (1) indicates that for a given aspect ratio (AR) this is achieved through minimizing skin friction drag ( $C_{D_0}$ ) and maximizing the wing efficiency  $e$  (which includes both planform and viscous effects). Prandtl's lifting line theory heralded the practical and accurate analysis of wing geometry effects, in essence an estimation of the second term of Eq. (1)

Received 5 August 2013; revision received 6 August 2014; accepted for publication 18 January 2015; published online 24 March 2015. Copyright © 2014 by the authors. Published by the American Institute of Aeronautics and Astronautics, Inc., with permission. Copies of this paper may be made for personal or internal use, on condition that the copier pay the \$10.00 per-copy fee to the Copyright Clearance Center, Inc., 222 Rosewood Drive, Danvers, MA 01923; include the code 1533-3868/15 and \$10.00 in correspondence with the CCC.

\*Associate Professor, Aerospace and Mechanical Engineering Department, Senior Member AIAA.

†Undergraduate Student, Aerospace and Mechanical Engineering Department, Student Member AIAA.

(ignoring sectional pressure drag) [1,2]. Within the geometrical confines of planar wings ( $AR > 5$ ), calculation revealed that a wing with an elliptical spanload distribution yielded the lowest inviscid drag due to lift [1]. The inviscid planform parameter ( $e_i$ ) reflects this efficiency and for this genre (planar and unswept) of wings has an upper bound of 1. An elliptic distribution is commonly associated with an elliptic planform shape. Elliptic loading can also be emulated at a selected loading condition using twist. Studies have implied that a larger chord near the wing tip may be required to generate a “true” elliptic load distribution [3]. With few exceptions (Supermarine Spitfire), manufacturing complexities and cost have negated the use of elliptic planforms.

Numerical lifting line theory as well as lifting surface methods show that the use of straight taper can yield wings with span efficiency factors close to elliptic (i.e.,  $e_i$  slightly below 1) [4]. A taper ratio of approximately 0.4 gives the highest efficiency for a given AR [4]. An increase in wing AR for a given taper ratio yields a systematic reduction in  $e_i$ . This does not imply that vortex drag increases, as the increase in the wing AR outweighs the drop in efficiency. As a trapezoidal wing AR gets higher, the spanload distribution becomes progressively flatter. This causes an increase in the load distributions curvature near the wing tips and thus greater strength of the shed trailing vorticity in the tip regions yielding a drop in  $e_i$ . For a given lift, a greater quantity of fluid is captured to generate the lift impulse such that the net kinetic energy of the downwash attenuates with an AR increase. Consequently, vortex drag lessens.

The effect of the taper ratio may be examined with reference to Fig. 1, which is based on data presented in this article. An impact of taper is a significant reduction in chord and thus  $Re$  as the wing tip is approached. At low Reynolds number ( $<250,000$ ) an airfoil zero or minimum (for cambered sections) drag coefficient shows a significant increase as  $Re$  drops [5]. Figure 1 shows a plot for  $\lambda = 0.2$  and 0.6 of the spanwise minimum drag coefficient for an untwisted wing with a S8036 airfoil as a function of  $Re$  ( $AR = 5.56$ ). Also presented is the spanwise variation of the minimum drag coefficient as a function of the local  $Re$  based on chord. As seen, the tip region experiences a disproportionate amount of the profile drag coefficient. A mean  $Re$  of 150,000 yields  $Re$  values of 66,666 in the tip vicinity. This results in extremely high values of the drag coefficient near the wing tips as indicated in Fig. 1. Although this would not explicitly reduce the wings planform efficiency  $e$ , it could reduce  $L/D$  by increasing  $C_{D_0}$ . Multiplication of the local  $C_d$  by  $qc$  to yield the local drag per meter indicates that the chord variation may compensate such that the local drag is dominated by the local chord.

An underlying premise in lifting line analysis is that the flow is inviscid. Thus, the drag due to lift contribution contains no (or negligible) sectional pressure drag contribution. At high Reynolds number this approximation is reasonable. At low  $Re$ , boundary layers are thick and the flow is generally dominated by laminar transitional bubbles — sectional pressure drag becomes a significant constituent of the drag breakdown. Taper also shifts loading outboard such that at low  $Re$  outboard wing sections may experience flow separation or excessively high pressure drag at moderate incidence (which could reduce  $e$ ). Thus, taper may cause a drop in  $e$  due to excessive outboard sectional pressure drag.

In an earlier study [5] the impact of AR on peak  $L/D$  and  $C_L^{3/2}/C_D$  for planar unswept rectangular wings was explored. It was shown that neglecting the impact of profile pressure drag yields optimal  $L/D$  ratios that essentially increase without bound as a function of AR. The inclusion of profile drag alters this outcome, such that identifiable peaks occur. The level of attainable leading-edge suction, which relates to the pressure component of the profile drag was the dominant parameter in the  $(L/D)_{max}$  location with respect to AR [5]. An increase in sectional pressure drag would drive the peak range and endurance parameter to a wing of lower AR. Sectional data examined in [5] indicated that profile pressure drag is comparatively invariant for  $Re > 60,000$ . Below this value, the pressure drag was observed to increase significantly suggesting that small tip chords at low  $Re$  would lead to increased pressure drag, with a corresponding impact on  $e$ .

The wide spread use of unmanned aerial vehicles (UAVs) has caused a significant increase in the research effort devoted to enhancing their efficiency and the understanding of their flow physics. It would be of value to the community to examine the impact of taper at low  $Re$  typical of a small UAV. In this article, an experimental program documenting the systematic variation of taper ratio for a wing with  $AR = 5.56$  is presented. Force balance and surface flow visualization results are documented. In addition, analytic and numerical estimates incorporating viscous effects are validated against the experimental data. Lifting line theory is extended to incorporate nonlinear section data facilitating simulation of the nonlinear lift curve slope and drag polar at low  $Re$ . A planform optimization is included yielding an optimal planform incorporating viscous effects.

### Equipment and Procedure

Five reflection plane wings with taper ratios of 1, 0.8, 0.6, 0.4, and 0.2 were tested, see Fig. 2. The quarter chord of the wings was unswept. All wings had a S8036 airfoil section (Fig. 2) and an aspect ratio of 5.56 to facilitate simulation using lifting line theory. The S8036 is a low  $Re$  section with moderate camber and thickness

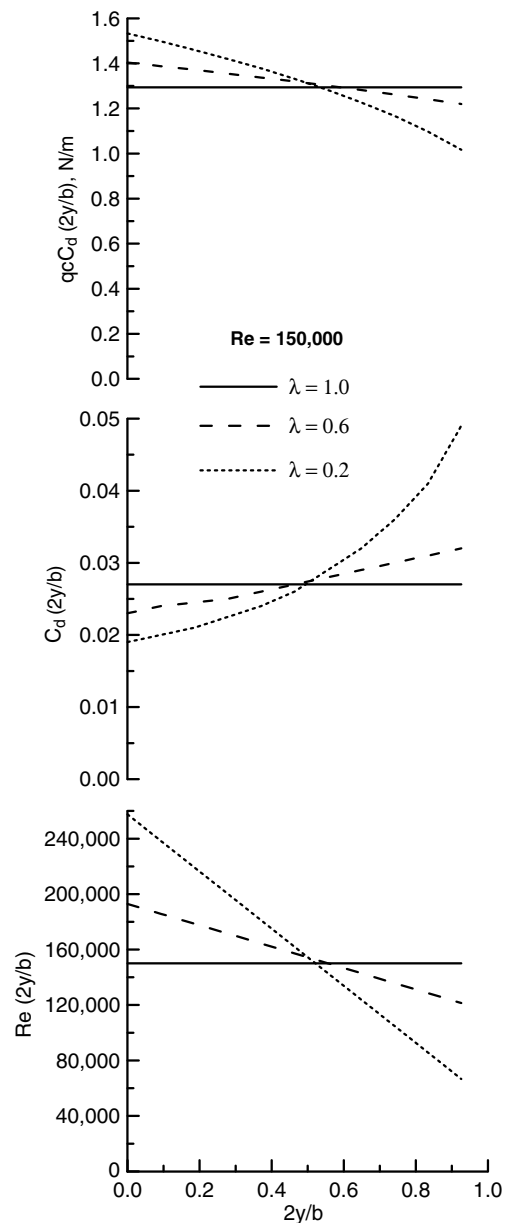


Fig. 1 Spanwise variation of drag, drag coefficient and  $Re$  for various taper ratios, S8036 section.

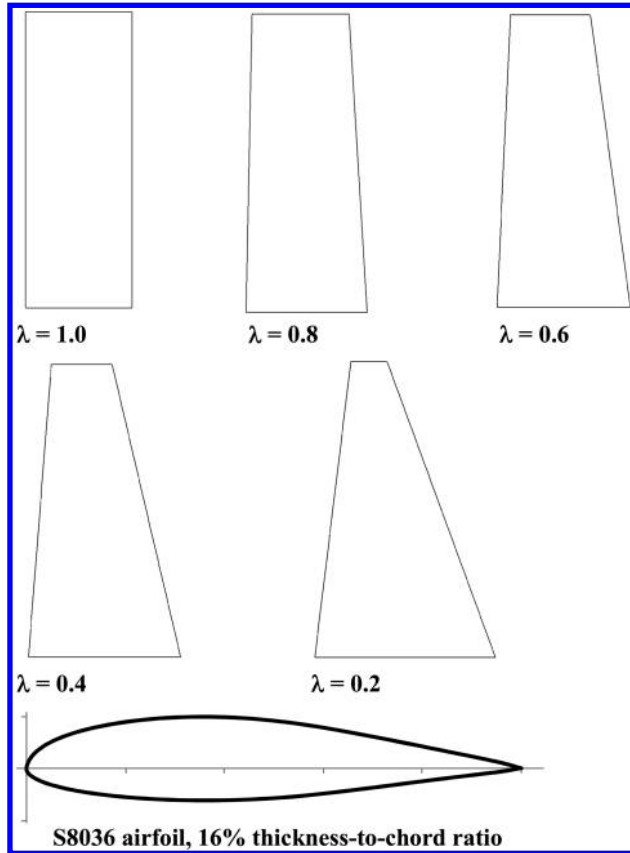


Fig. 2 Geometry of wind-tunnel models and airfoil section. Flow direction is from left to right.

(16%). The rectangular wing ( $\lambda = 1$ ) had an additional end piece that could be attached to the wing such that it would span the test section of the wind tunnel (0.5 mm gap between the wing and side wall). This would allow the sectional characteristics of the profile to be examined. The wings were created in CATIA and rapid prototyped yielding acrylonitrile butadiene styrene models. All wing tips were blunt. Wing finishing encompassed sanding and coating with gloss black paint. The wing planform area ( $0.016 \text{ m}^2$ ) was similar for all models. The reflection plane wingspan was 0.209 m.

Wind-tunnel testing was undertaken using an open circuit 0.3048 m by 0.3048 m ELD wind tunnel. An external 3-component platform balance was used to measure the loads experienced by the wings. The angle of attack is set using a stepper motor controlled by a Velmex controller. The voltage outputs from the load cells (Transducer Techniques) are digitized using a National Instruments 14 bit analog-to-digital board. Acquisition is accomplished using a Labview interface that reads and processes all inputs. The program low pass filters all signals at 20 Hz using a Butterworth filter. All presented data points represent 1000 averaged samples. From calibration, the balance has a demonstrated accuracy within 0.01 N of the applied load. Flow visualization was also implemented using titanium dioxide suspended in kerosene and linseed oil.

Wing testing was undertaken at  $Re = 100,000$  and  $150,000$  based on the mean chord length of 0.075 m. Characterization of the airfoil behavior (using the additional end piece) was undertaken at  $Re = 40,000, 60,000, 80,000, 100,000, 125,000, 150,000, 175,000,$  and  $200,000$ . Testing involved an angle of attack sweep from  $-4$  to  $20$  deg in two deg increments. Wall corrections were applied using the method of Shindo [6] for finite wing solid and wake blockage and those described in [7] for the downwash. A value of 0.92 was used for the downwash parameter [7]. Corrections for solid and wake blockage were small; with a maximum coefficient change of 1.9% at high load conditions. Corrections due to downwash were larger, peaking at approximately 14%. The corrections were adjusted [7] to account for the use of reflection plane wings as appropriate.

## Results and Discussion

In this section, two theoretical approaches are presented to facilitate determination of the viscous and inviscid drag of a tapered wing at low  $Re$ . Subsequently the experimental data is examined and then compared with theory.

### Theory—Analytic

In [8] a method is presented that allows the incorporation of sectional pressure drag into a finite wing drag estimate. The approach assumes knowledge of the two-dimensional (2-D) polar for the airfoil section and uses it to extract the variation of the airfoil's leading-edge suction with incidence. A loss of leading-edge suction is interpreted as a rise in pressure drag. Consult [8] for further background on the method. The drag due to lift (incorporating vortex and sectional pressure drag) of the wing is estimated using [8]

$$C_{DL} = (1 - \eta)C_{L\alpha} \left( \frac{C_L}{C_{L\alpha}} + \alpha_{ZL} \right)^2 + \frac{C_{L\alpha}^2}{\pi A R e_i} \left( \eta \left( \frac{C_L}{C_{L\alpha}} + \alpha_{ZL} \right)^2 - 2 \left( \frac{C_L}{C_{L\alpha}} + \alpha_{ZL} \right) \alpha_{ZL} + \alpha_{ZL}^2 \right) \quad (2)$$

where the attainable leading-edge suction is estimated using experimental data or simulation for the airfoil section and is given by

$$\eta = 1 - \frac{(C_d - C_{d \min})}{C_l \left( \frac{C_l}{C_{l\alpha}} + \alpha_{ZL} \right)} \quad (3)$$

For a symmetrical section  $\alpha_{ZL} = 0$ . Estimates for  $C_{l\alpha}$  may be made using any suitable panel method (e.g., Xfoil, Javafoil, etc.). The finite wing characteristics ( $C_{L\alpha}$  and  $e_i$ ) can be established using a vortex lattice/panel method (AVL, Tornado, XFLR5, etc.) or a numerical lifting line code, depending on the wing's geometry. For a tapered wing, application of Eq. (3) would use an airfoil drag polar at the  $Re$  of the wing's average chord. The validity of this simplification will be examined later. Note that this method does not estimate the zero lift or minimum drag coefficient, which is primarily caused by skin friction. Thus,  $C_{D0}$  or  $C_{D \min}$  needs to be determined from experiment or other means.

The zero lift or minimum drag coefficient for a tapered wing may be estimated based on knowledge of the sectional characteristics. The minimum or zero lift drag of the airfoil section may be approximated as

$$C_{d \min} = A(Re)^\beta \quad (4)$$

The local Reynolds number may be written as

$$Re(y) = \frac{\rho V c(y)}{\mu} \quad (5)$$

For a straight tapered wing, the variation of the chord is given by

$$c(y) = c_r [1 - (1 - \lambda)2y/b] \quad (6)$$

The minimum or zero lift drag for the wing may be estimated (excluding twist) as

$$C_{D \min} = \frac{2}{S} \int_0^{b/2} C_{d \min}(y) c(y) dy \quad (7)$$

which after substitution yields

$$C_{D \min} = \frac{2}{S} \int_0^{b/2} A(Re)^\beta c_r [1 - (1 - \lambda)2y/b] dy \quad (8)$$

Substituting for  $Re$  and integrating gives

$$C_{D \min} = \frac{2}{S} A \left( \frac{\rho V}{\mu} \right)^\beta \left( \frac{1}{2} b c_r^{(1+\lambda)} \right) \frac{[\lambda^{(2+\beta)} - 1]}{[(\lambda - 1)(2 + \beta)]} \quad (9)$$

Equation (9) allows the estimation of the wing's zero lift or minimum drag coefficient provided the variation of the sectional characteristics as a function of Reynolds number are known. Note that Eq. (9) is valid for  $\lambda < 0.999$ . The total drag of the wing is given by Eq. (2) plus Eq. (9).

**Theory—Extended Lifting Line**

In this section lifting line theory is extended to incorporate nonlinear viscous lift and drag effects. The method was developed to work in conjunction with an optimizer if desired. The formulation solves for the  $C_D$  and  $\alpha$  from a user specified  $C_L$ . The wing area and AR are prescribed and fixed. To obtain the entire nonlinear 3-D lift curve or drag polar the process must be repeated for each desired  $C_L$  value. The wingspan may be calculated using

$$b = \sqrt{S \times AR} \quad (10)$$

and used to calculate the mean geometric chord

$$\bar{c} = S/b \quad (11)$$

Following numerical lifting line theory, the number of spanwise divisions provides the terms in the Fourier series

$$N = r - 1 \quad (12)$$

Calculating the angular location of the spanwise stations, from 0 to  $\pi$ , with  $n$  ranging from 1 to  $N$

$$\theta_n = \frac{n\pi}{r} \quad (13)$$

This formulation packs the stations closer to the tips, as is common in lifting line theory. The location of each station relative to the midplane is given by [9]

$$y_n = \frac{-b \cos(\theta_n)}{2} \quad (14)$$

Normalizing the  $y$  coordinates relative to the span yields

$$\eta_n = \left| \frac{2y_n}{b} \right| \quad (15)$$

Straight tapered wings were experimentally evaluated in this study. Consequently, the root chord length follows as

$$c_r = \frac{2\bar{c}}{1 + \lambda} \quad (16)$$

With a local chord length of [4]

$$c_n = c_r(1 - \eta_n(1 - \lambda)) \quad (17)$$

The local chord length along with the test conditions provide the Reynolds number at each station

$$Re_n = \frac{\rho_\infty V_\infty c_n}{\mu_\infty} \quad (18)$$

The experimental wind-tunnel data for the airfoil is best curve fitted to provide smooth sectional lift curve slopes. This is necessary as higher order polynomial functions can provide better behaved differentiable values (than experimental) at all possible points. These

fitted polynomials are used in lieu of the raw experimental data for the  $C_l$  verse  $\alpha$  data only. The sectional drag data does not require curve fitting.

The sectional lift curve slope and sectional  $\alpha_{ZL}$  is found iteratively. This iteration is necessary as the lifting line solution is closely coupled with the 2-D behavior of the airfoil. Low  $Re$  flows exhibit highly nonlinear lift curve slopes over a range of angles attack, requiring iteration. The values for both (lift curve slope and zero lift angle) are initially assumed to be  $2\pi/\text{rad}$  and 0 rad, respectively. Following the solution of the sectional  $C_l$  values, the entire lifting line solution and interpolation is iterated.

Conventional formulations of lifting line theory solve the Fourier coefficients and the  $C_L$  given an angle of attack. However, with manipulation, the Fourier coefficients and angle of attack may be solved from the  $C_L$ . Initiating with a common form of the lifting line equation [10]

$$\frac{c_n C_{l_{\alpha_n}} \sin(\theta_n)(\alpha + \alpha_{\text{geo}_n} - \alpha_{ZL_n})}{4b} = \sum_{i=1}^N \sum_{n=1}^N A_n \sin(i\theta_n) \left( \sin(\theta_n) + \frac{ic_n C_{l_{\alpha_n}}}{4b} \right) \quad (19)$$

Now grouping terms that may be evaluated at the same spanwise location

$$k_n = \frac{c_n C_{l_{\alpha_n}}}{4b} \quad (20)$$

A characteristic of the Fourier series enables the  $C_L$  to be proportional only to the first Fourier coefficient [10]

$$C_L = A_1 \pi AR \quad (21)$$

Rearranging Eq. (21)

$$A_1 = \frac{C_L}{\pi AR} \quad (22)$$

By substituting Eq. (20) and separating the first Fourier coefficient from the summation

$$k_n \sin(\theta_n)(\alpha + \alpha_{\text{geo}_n} - \alpha_{ZL_n}) = A_1 \sin(\theta_n)(\sin(\theta_n) + k_n) + \sum_{n=1}^N \left[ \sum_{i=2}^N A_i \sin(i\theta_n)(\sin(\theta_n) + ik_n) \right] \quad (23)$$

By rearranging with known terms on the left and unknowns on the right, and substituting Eq. (22)

$$k_n \sin(\theta_n)(\alpha_{\text{geo}_n} - \alpha_{ZL_n}) - \frac{C_L}{\pi AR} \sin(\theta_n)(\sin(\theta_n) + k_n) = \sum_{n=1}^N \left[ \sum_{i=2}^N A_i \sin(i\theta_n)(\sin(\theta_n) + ik_n) - k_n \sin(\theta_n)\alpha \right] \quad (24)$$

To solve via matrix methods the left side becomes the vector

$$\text{LHS} = \begin{bmatrix} k_1 \sin(\theta_1)(\alpha_{\text{geo}_1} - \alpha_{ZL_1}) - \frac{C_L}{\pi AR} \sin(\theta_1)(\sin(\theta_1) + k_1) \\ \vdots \\ k_N \sin(\theta_N)(\alpha_{\text{geo}_N} - \alpha_{ZL_N}) - \frac{C_L}{\pi AR} \sin(\theta_N)(\sin(\theta_N) + k_N) \end{bmatrix} \quad (25)$$

With the known coefficients on the right side becoming the matrix

$$\text{RHS} = \begin{bmatrix} \sin(2\theta_1)(\sin(\theta_1) + 2k_1) & \cdots & \sin(N\theta_1)(\sin(\theta_1) + Nk_1) & -k_1 \sin(\theta_1) \\ \vdots & \ddots & \vdots & \vdots \\ \sin(2\theta_N)(\sin(\theta_N) + 2k_N) & \cdots & \sin(N\theta_N)(\sin(\theta_N) + Nk_N) & -k_N \sin(\theta_N) \end{bmatrix} \quad (26)$$

Solving for the unknown Fourier coefficients as well as the angle of attack results in the vector

$$\begin{bmatrix} A_2 \\ \vdots \\ A_N \\ \alpha \end{bmatrix} = \text{RHS}^{-1} \text{LHS} \quad (27)$$

With the Fourier coefficients determined, the trigonometric series follows [11]

$$\left(\frac{C_l c}{b}\right)_n = \sum_{n=1}^N 4A_n \sin(n\theta_n) \quad (28)$$

The results of this series are used to solve for the sectional lift coefficient [11]

$$C_l = \frac{b \left(\frac{C_l c}{b}\right)_n}{c_n} \quad (29)$$

Using the sectional lift coefficient at each spanwise station the accompanying local sectional lift curve slope is solved by interpolation of the differentiation of the preceding polynomials based on local  $Re$ . The  $\alpha_{ZL}$  is determined via the solved  $C_l$  and the sectional lift curve slope, the local angle of attack  $\alpha_{Cl}$ , which is easily found once the local  $C_l$  is identified

$$\alpha_{ZL} = \alpha_{Cl} - \frac{C_l}{C_{l\alpha}} \quad (30)$$

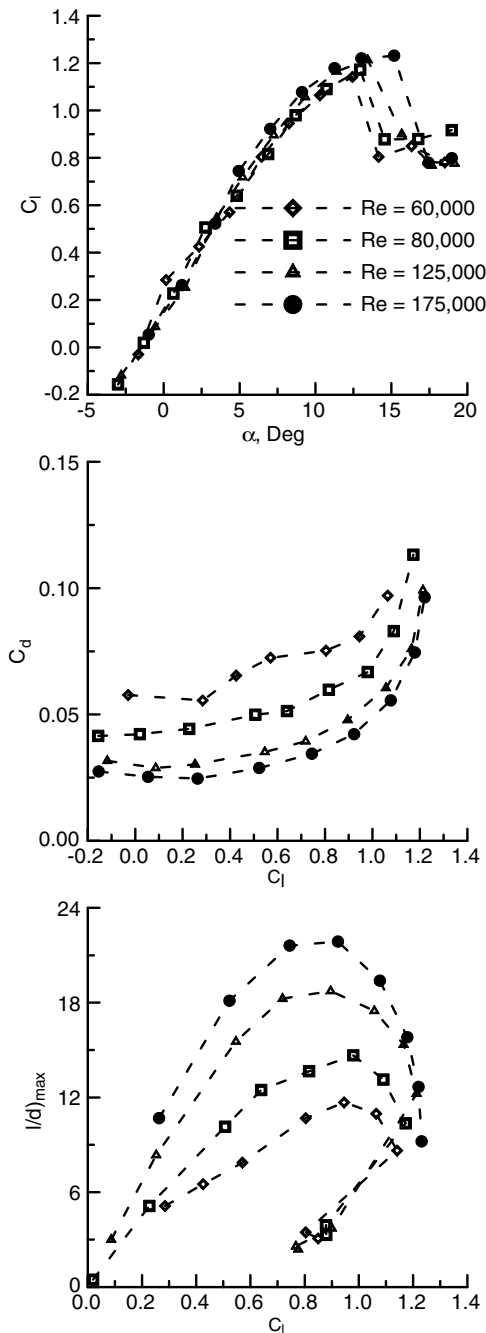


Fig. 3 Effect of  $Re$  on behavior of S8036 airfoil.

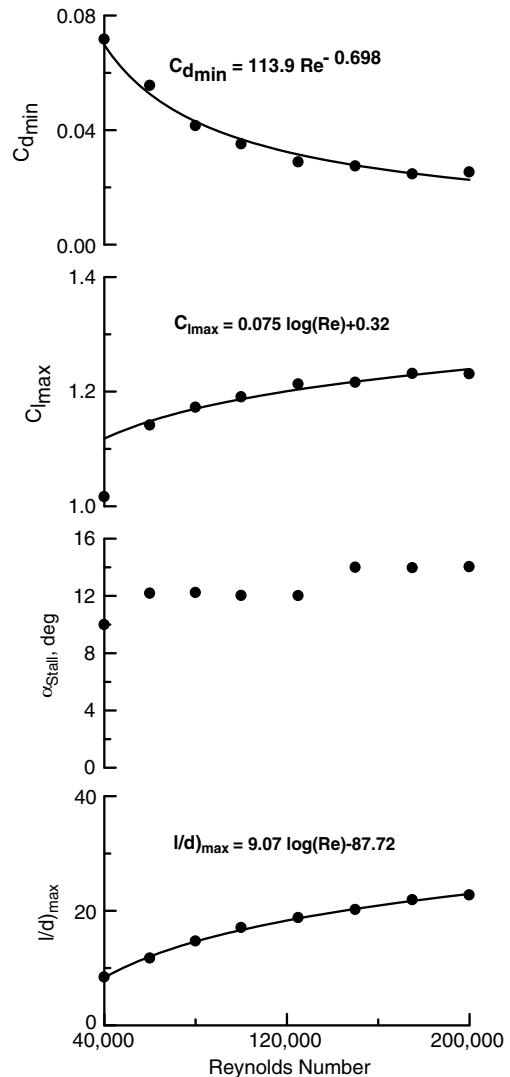


Fig. 4 Performance summary characterizing effect of  $Re$  on S8036 airfoil.

Equations (24–30) are iterated until the values of the sectional lift curve slope and sectional  $\alpha_{ZL}$  converge to within a prescribed tolerance.

Once complete, the following multiplier [11] is used throughout the determination of several coefficients ( $m$  is not an index)

$$\eta_m = \frac{\pi \sin(\theta_n)}{2r} \tag{31}$$

Once the final angle of attack is attained, the induced angle of attack, in rad, is found through [11]

$$\alpha_i = \sum_{n=1}^N \frac{nA_n \sin(n\theta_n)}{\sin(\theta_n)} \tag{32}$$

and is used for the sectional vortex drag [11]

$$C_{d_v} = C_l \alpha_i \tag{33}$$

An integration of the sectional vortex drag over the entire wing yields the total vortex drag [11]

$$C_{D_v} = \sum_{n=1}^N C_{d_{v_n}} AR \eta_m \tag{34}$$

From the local  $C_l$ , a lookup of the local airfoil sectional drag coefficient  $C_d$  values is found for two closest Reynolds numbers and linearly interpolated. For rapid iteration, linear interpolation is preferred; other forms of interpolation provide negligible differences in final values at the expense of greater computational effort. The three-dimensional (3-D) wing profile drag is found through an integration of the sectional profile drag [11]

$$C_{D_{\text{profile}}} = \sum_{n=1}^N \frac{C_{d_n} c_n \eta_m}{\bar{c}} \tag{35}$$

Finally, combining drag values yields the total drag of the wing

$$C_D = C_{D_{\text{profile}}} + C_{D_v} \tag{36}$$

The particular steps for this method are enumerated below:

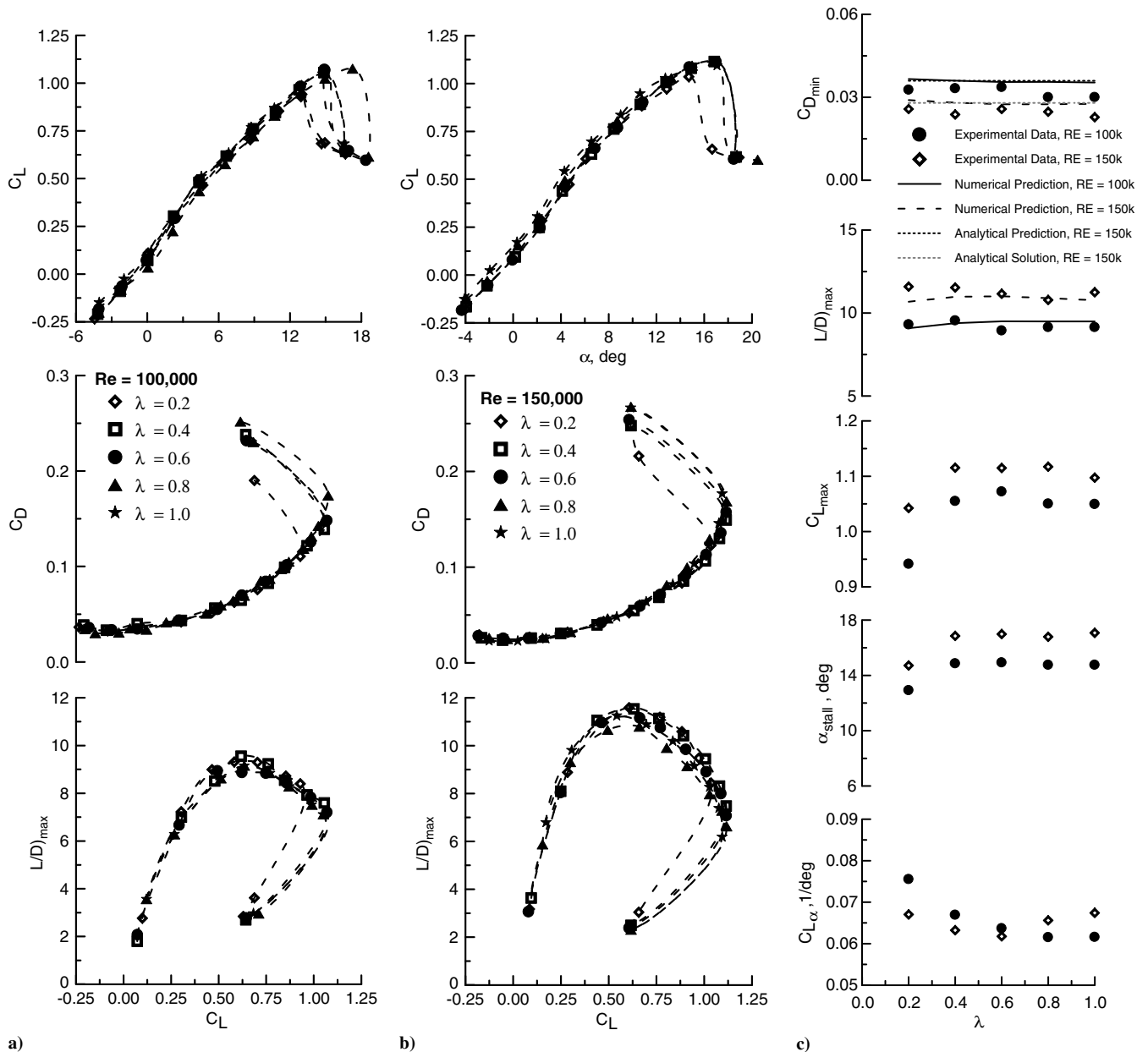


Fig. 5 Effect of taper ratio on longitudinal aerodynamic forces: a)  $Re = 100,000$ , b)  $Re = 150,000$ , and c) summary of influence of taper ratio on performance characteristics.

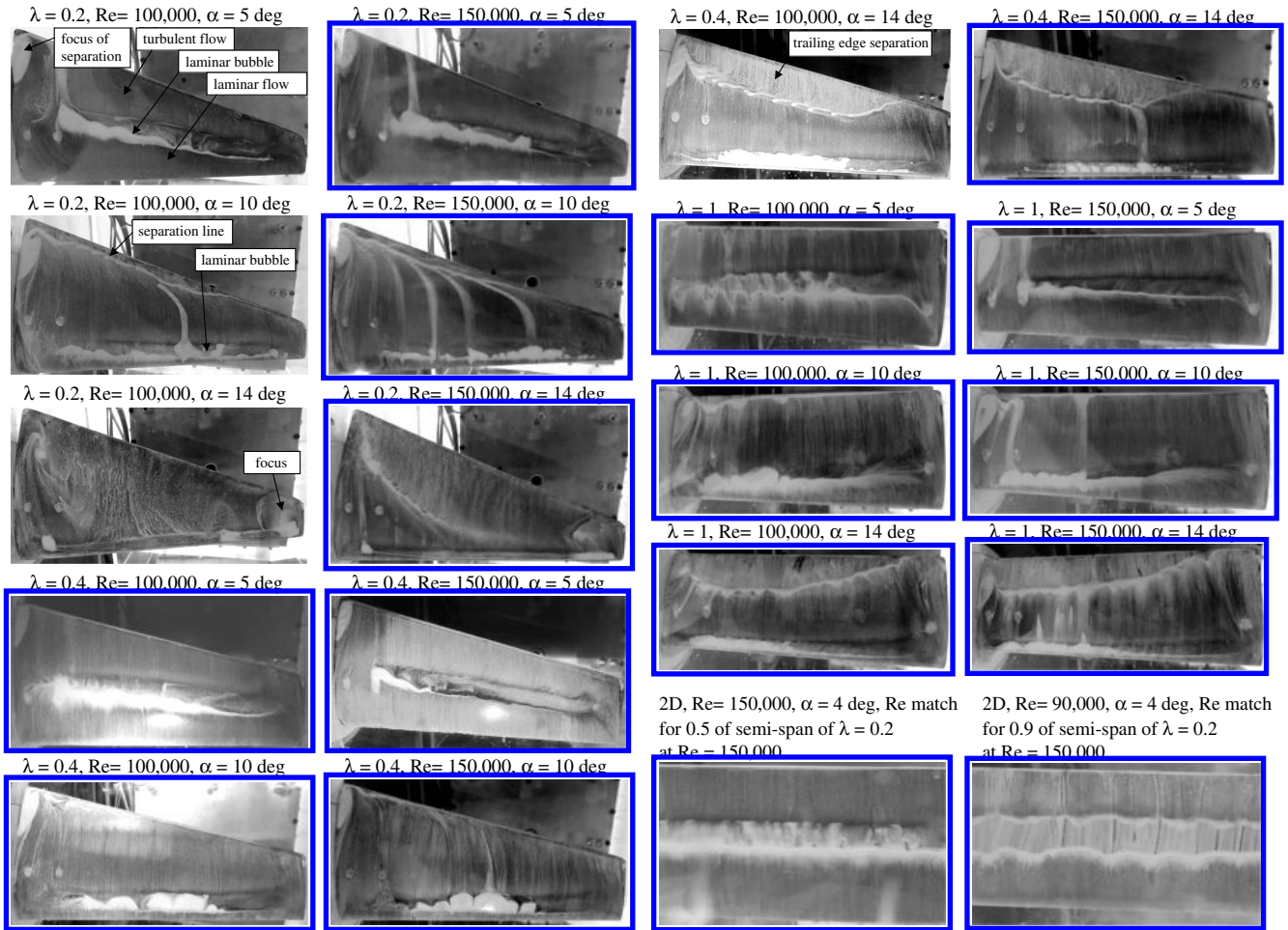


Fig. 6 Effect of  $\alpha$  and  $Re$  on Titanium Dioxide rendered skin friction patterns (flow from bottom to top).

- 1) Select wing area  $S$  and AR. Calculate the wingspan  $b$  and mean geometric chord  $\bar{c}$ .
- 2) Select the number of terms in the Fourier series (20) and then calculate the spanwise divisions  $r$ .
- 3) Calculate the angular location of the stations  $\theta_n$ .
- 4) Calculate and normalize the spanwise evaluation stations  $y_n$ .
- 5) Calculate the root, local chord and  $Re$  at each spanwise station.
- 6) Curve fit using polynomials (or similar) sectional 2-D airfoil lift data encompassing the  $Re$  range expected across the wing.

7) Initial values for the 2-D lift curve slope and zero lift angle of attack are assumed, generally  $2\pi$  and 0, and later iterated. Iteration occurs until the values are within a close prescribed tolerance.

8) Equation (24) is solved to produce the unknown Fourier coefficients  $A_n$ , which may be solved through the described matrix method using the local chord lengths  $c_n$ , the local 2-D lift curve slope  $C_{lan}$ , the local 2-D zero lift angle of attack  $\alpha_{ZL}$ , wingspan  $b$ , and any geometric twist applied  $\alpha_{GEO}$ .

Table 1 Effect of taper ratio and  $Re$  on bubble characteristics,  $\alpha = 5$  deg

Parameter	$2y/b = 0.27, Re = 100,000$	$2y/b = 0.81, Re = 100,000$	$2y/b = 0.27, Re = 150,000$	$2y/b = 0.81, Re = 150,000$
$x_f/c(y)$ ( $\lambda = 0.2$ )	0.35	0.23	0.35	0.26
$x_b/c(y)$ ( $\lambda = 0.2$ )	0.52	0.58	0.53	0.54
$x_{bubble}/c(y)$ ( $\lambda = 0.2$ )	0.17	0.35	0.19	0.28
$x_f/c(y)$ ( $\lambda = 0.4$ )	0.32	0.34	0.29	0.37
$x_b/c(y)$ ( $\lambda = 0.4$ )	0.51	0.62	0.48	0.59
$x_{bubble}/c(y)$ ( $\lambda = 0.4$ )	0.19	0.18	0.18	0.23
$x_f/c(y)$ ( $\lambda = 1$ )	0.38	0.40	0.38	0.42
$x_b/c(y)$ ( $\lambda = 1$ )	0.56	0.60	0.57	0.61
$x_{bubble}/c(y)$ ( $\lambda = 1$ )	0.18	0.20	0.19	0.19

Table 2 2-D and 3-D bubble characteristics,  $\alpha = 4$  deg

Parameter	$2y/b = 0.9, Re_n = 90,000$	2-D, $Re = 90,000$	$2y/b = 0.5, Re_n = 150,000$	2-D, $Re = 150,000$
$x_f/c(y)$ ( $\lambda = 0.2$ )	0.26	—	0.36	—
$x_b/c(y)$ ( $\lambda = 0.2$ )	0.55	—	0.56	—
$x_{bubble}/c(y)$ ( $\lambda = 0.2$ )	0.29	—	0.20	—
$x_f/c(y)$ (2-D)	—	0.38	—	0.40
$x_b/c(y)$ (2-D)	—	0.65	—	0.65
$x_{bubble}/c(y)$ (2-D)	—	0.28	—	0.25

9) The local  $C_l$  values are solved using Eqs. (28) and (29) using the Fourier coefficients  $A_n$  from step 8.

10) These  $C_l$  values are then used to determine the local 2-D lift curve slope and the local 2-D zero lift angle of attack. Variations in the Reynolds number require interpolation of the applicable values based on the local Reynolds numbers. The lift curve slopes can be found through differentiation of the polynomial curve fits found in step 6. Using these lift curve slopes the zero lift angle of attack is found through Eq. (30).

11) Steps 8 through 10 are repeated iteratively until the lift curve slopes converge to within a prescribed tolerance of the prior value. This provides reasonable assurance that the  $C_l$  distribution is accurate.

12) Next, the multiplier  $\eta_m$  is solved for each station using Eq. (31).

13) The local induced angle of attack  $\alpha_i$  is calculated using Eq. (32), using the Fourier coefficients  $A_n$  from step 8.

14) The induced angle of attacks  $\alpha_i$  from step 14 are then combined with the local  $C_l$  to calculate the local vortex drag  $C_{dv}$  using Eq. (33). Summing these local vortex drag contributions  $C_{di}$  the multiplier  $\eta_m$ , and the AR are used in Eq. (34) to solve for the vortex drag for the finite wing  $C_{Di}$ .

15) The local profile drag coefficient  $C_{dprofile}$  values are found through a combination of linear interpolation of the 2-D drag polar,  $C_{dprofile}$  values based from the local  $C_l$  values found in step 9 and based on the local Reynolds number.

16) These  $C_{dprofile}$  contributions are integrated over the span using Eq. (35) to produce the  $C_{Dprofile}$  of the finite wing. This equation weights the local chord length,  $c_n$ , to the mean geometric chord.

17) Finally, summing the values from steps 16 and 17 produces the total finite wing drag coefficient  $C_D$ .

The method described above was verified using computations in Sivells and Neely [11,12]. Although not included explicitly due to space considerations, the method closely matched with that in [12]. The test article had an AR = 9, no washout, a taper ratio of 0.4, and a Reynolds number of  $4.4 \times 10^6$ .

Note that a fundamental difference between the analytic and numerical lifting line theory approaches is in the estimate of the sectional pressure drag. The analytic approach combines the sectional pressure and finite wing inviscid vortex drag into a total drag due to lift term ( $C_{DL}$ ). The numerical approach, following that of [11] combines the viscous drag into a single term ( $C_{Dprofile}$ ) separate from the inviscid vortex drag ( $C_{Dv}$ ).

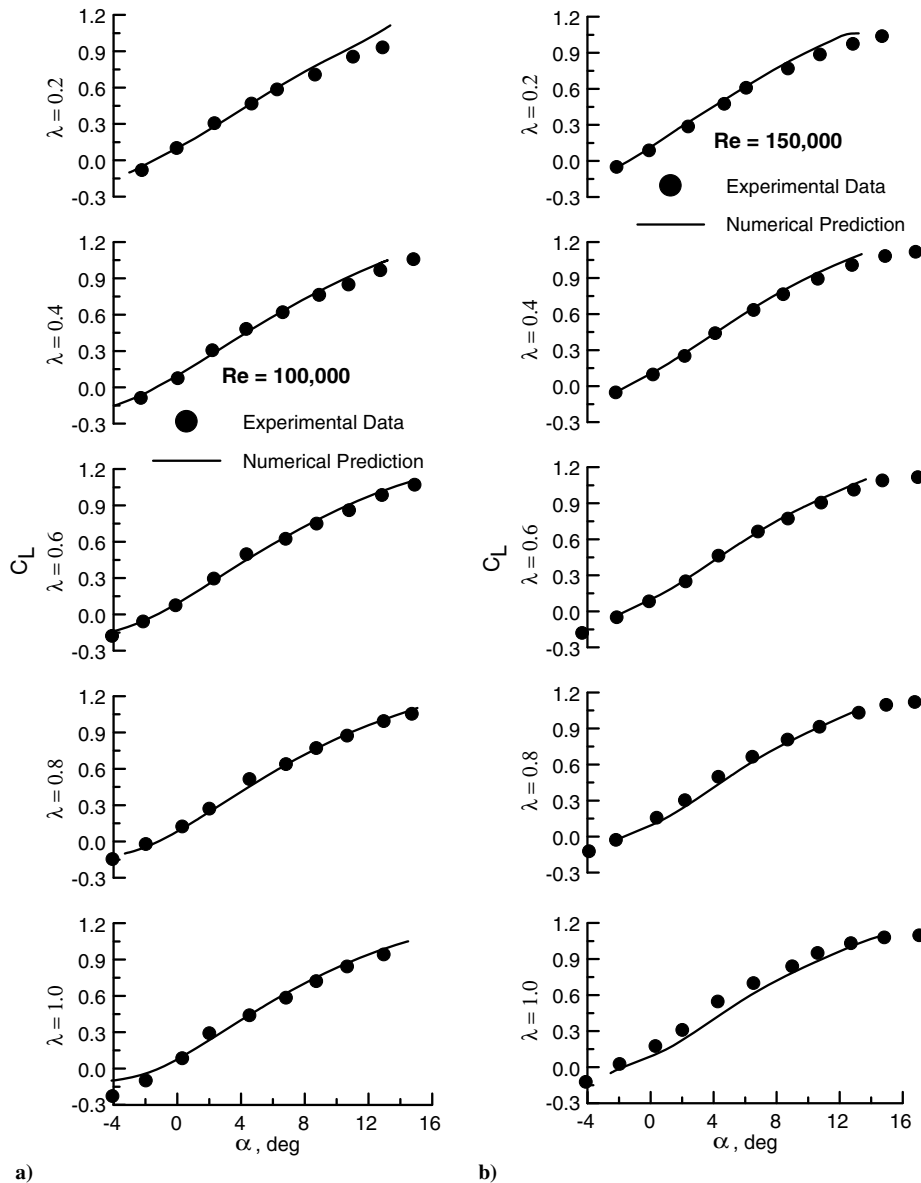
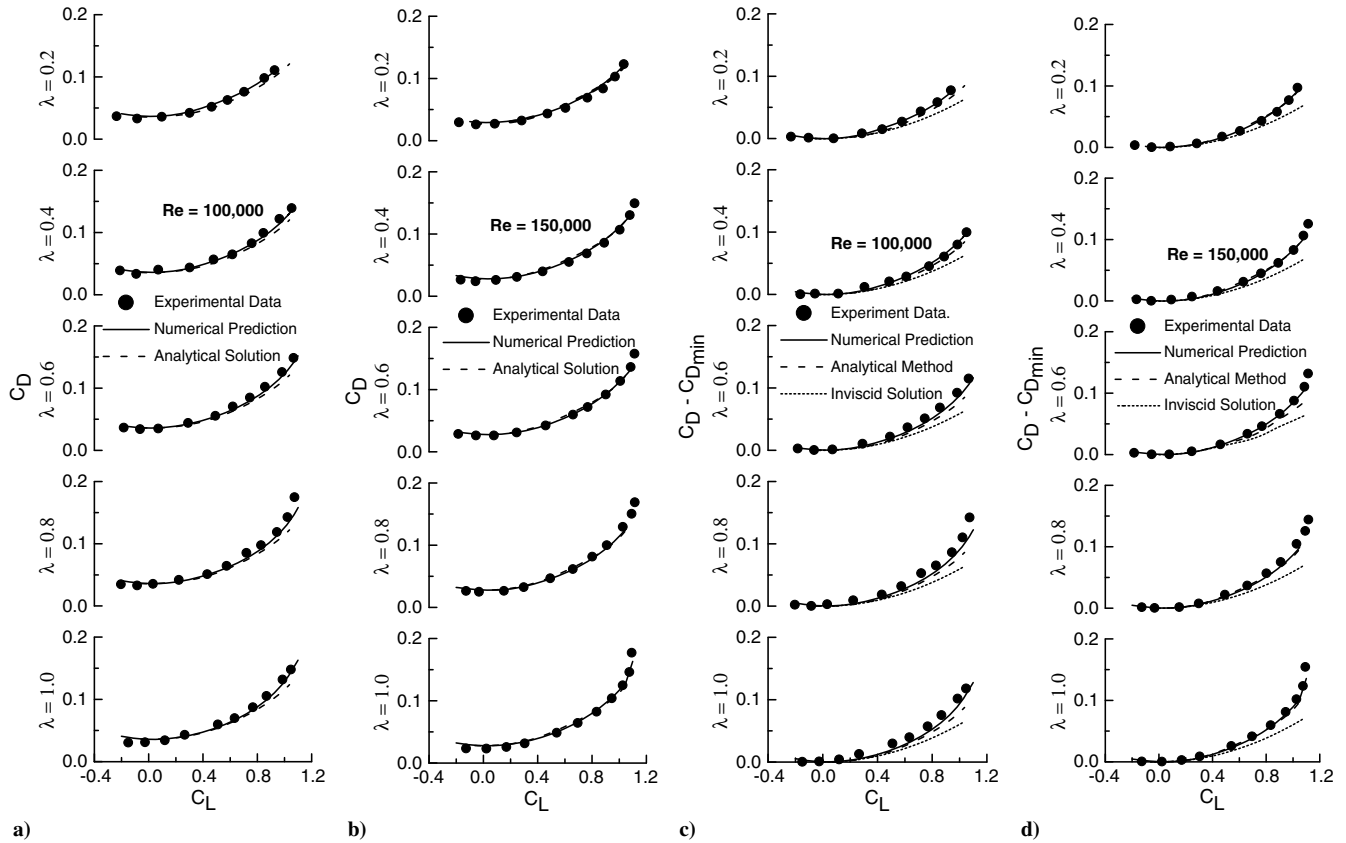


Fig. 7 Comparison of nonlinear numerical lifting line theory and experiment: a)  $Re = 100,000$  and b)  $Re = 150,000$ .



**Fig. 8** Comparison of analytic theory and nonlinear numerical lifting line theory with experiment, total  $C_D$ : a)  $Re = 100,000$ , and b)  $Re = 150,000$ , and  $C_D - C_{D\min}$ , c)  $Re = 100,000$ , and d)  $Re = 150,000$ .

### Optimization

In an effort to determine the best planform for drag minimization accounting for planform and viscous effects, an optimizer was implemented. To allow for a wide range of possible planform shapes the following equation was used instead of Eqs. (16) and (17) in the numerical method

$$c_n = c_r(1 - \eta_n^p)^q + c_t \eta_n \quad (37)$$

Equation (37) yields a variety of permissible planform shapes including elliptic and rectangular. Using Eq. (37), constraints for optimizing the planform must be implemented. In this implementation the wing area and aspect ratio, and thus the wingspan must be conserved. By integrating equation (37) over the semispan

$$\frac{S}{2} = \int_0^{\frac{b}{2}} c(y) dy = \int_0^{\frac{b}{2}} [c_r(1 - \eta_n^p)^q + c_t \eta_n] dy \quad (38)$$

The resultant function includes a hypergeometric series

$$\begin{aligned} \frac{S}{2} &= \int_0^{\frac{b}{2}} \left[ c_r \left( 1 - \left( \frac{2y}{b} \right)^p \right)^q + c_t \frac{2y}{b} \right] dy \\ &= \frac{bc_r}{4} + \frac{bc_r}{2} {}_2F_1 \left( -q, \frac{1}{p}; 1 + \frac{1}{p}; 1 \right) \end{aligned} \quad (39)$$

When used in a constrained optimizer the aspect ratio and wing area are conserved throughout the process. Additionally, the following constraints was implemented

$$c_r > 0 \quad \text{and} \quad c_t > 0 \quad (40)$$

The MATLAB optimization toolbox was used. The Sequential Quadratic Programming (SQP) algorithm of `fmincon` was chosen. The SQP algorithm is a gradient-based method that adheres to all constraints throughout the iteration process [13]. Several different initial starting planforms were attempted to ensure convergence to the same solution planform. Initial gradients were not user supplied.

### Experimental Results

#### Sectional-Airfoil

The sectional aerodynamic characteristics of the S8036 profile are examined in Fig. 3. Testing encompassed a  $Re$  sweep from 40,000 to 200,000. For graphical clarity, some data sets have been omitted in the plot. As seen, the impact of  $Re$  is primarily associated with  $C_d$ . Increasing  $Re$  yields a reduction in boundary layer thickness and a contraction of the laminar bubble for a given incidence [14], yielding a reduction in  $C_d$ . Drag coefficient attenuation is reflected in significant improvements in the maximum lift to drag ratio with  $Re$ . The curvature of the drag polar, relating to sectional pressure drag is observed to be similar for  $Re \geq 125,000$ . For  $Re$  ranging from 125,000 to 200,000 the impact of  $Re$  for this airfoil is a  $C_{d\min}$  shift with little change in the  $C_l$  dependence. The appearance of  $C_{d\min}$  at  $C_l > 0$  (as would be expected for a cambered airfoil) is observed to be  $Re$  dependent ( $Re = 80,000$  to  $175,000$ ), indicating a reduction in drag due to lift (pressure drag) due to bubble contraction and a lessening of upper surface trailing-edge separation (as indicated through Xfoil<sup>‡</sup> simulation).

A summary of airfoil characteristics is presented in Fig. 4 explicitly showing  $Re$  dependence. Reynolds number effects manifest primarily in the drag coefficient. The minimum value of the drag coefficient is seen to drop rapidly for  $Re < 150,000$  and then flatten. As indicated by the  $C_{d\min}$  curve fit, the drag rise with  $Re$  is slower than for purely laminar flow (i.e.,  $\propto Re^{-0.5}$ ) and is due to the mixed

<sup>‡</sup>Data available online at <http://web.mit.edu/drela/Public/web/xfoil/> [accessed 1 May 2013].

(laminar transition-bubble turbulent) nature of the flow. Lift based characteristics ( $C_{l,max}$  and  $\alpha_{Stall}$ ) improve markedly as the  $Re$  increases above 40,000. This is reflective of elimination of large scale laminar separation through natural transition of the separated shear layer causing re-attachment and consequently the formation of a bubble. The dramatic reduction in  $C_{d,min}$  causes a systematic improvement in  $l/d)_{max}$  with a logarithmic dependency shown.

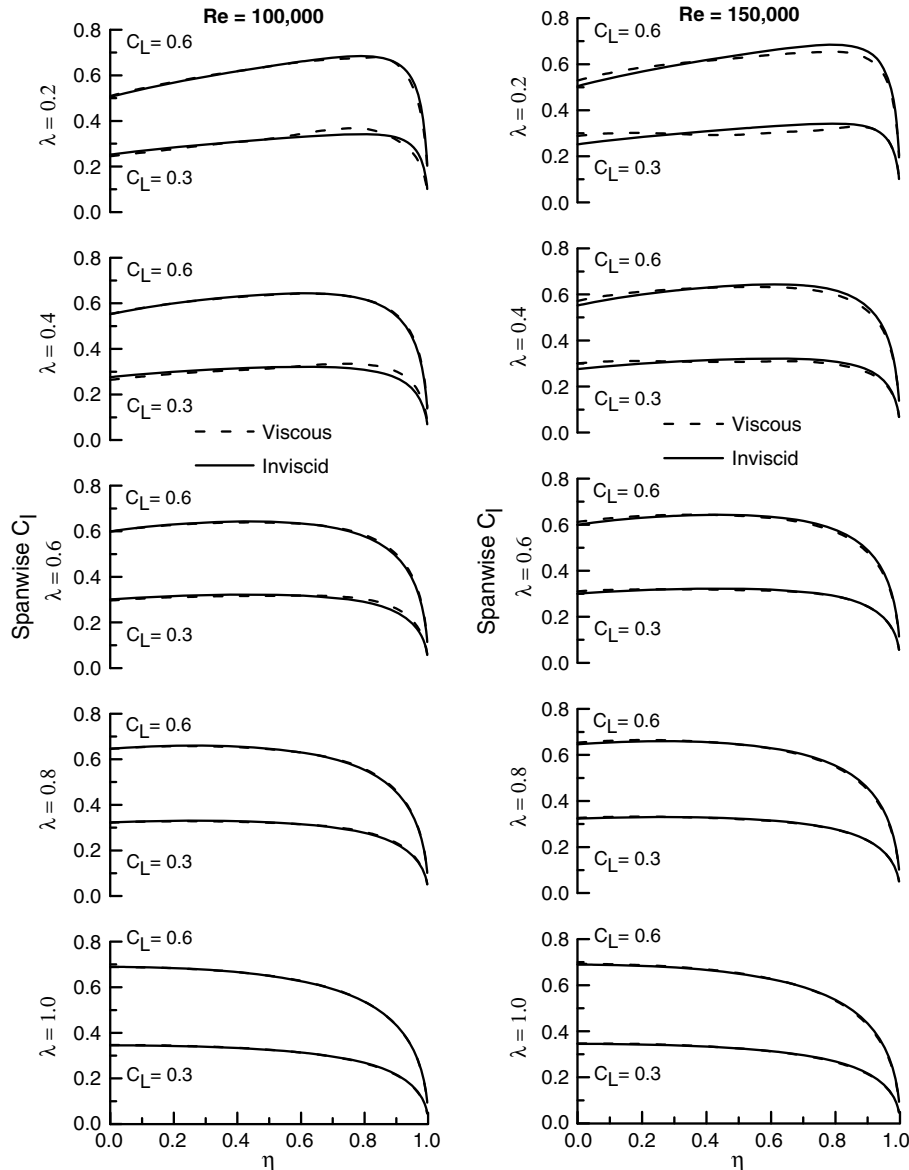
**Finite-Wing**

Figure 5 presents the impact of taper ratio on the longitudinal aerodynamic characteristics of the wing. For either  $Re$ , the data does not reveal an overwhelming impact of taper ratio (Figs. 5a and 5b). Wing stall characteristics are insensitive to  $\lambda$  in this  $Re$  range. The maximum lift to drag ratio favors  $\lambda = 0.2$  to  $0.4$ . Figure 5c displays a summary characterizing pertinent performance parameters as affected by taper and  $Re$ . A reduction in the taper ratio causes a net increase in the wing's lift curve slope (measured over the  $-4 < \alpha < 4$  deg interval) for  $Re = 100,000$  although this trend is inconclusive for  $Re = 150,000$ . Both  $C_{L,max}$  and  $\alpha_{Stall}$  favor a lower  $\lambda$  of  $0.4$  to  $0.6$  while  $\lambda = 0.2$  decreases both of these quantities markedly. The maximum lift to drag ratio does not show any marked trends, although it may be seen that  $\lambda = 0.4$  performs best. The minimum drag coefficient increases as taper reduces, due to an outboard sectional

drag coefficient penalty. Also included on the plots are predictions from the extended numerical lifting line theory ("Numerical Prediction") and the analytic method [Eq. (9)]. The minimum drag estimates obtained using Eq. (9) and lifting line theory show close accord and agreement with experiment. The numerical estimates of  $(L/D)_{max}$  are also in good agreement with experiment.

Skin friction patterns, rendered using Titanium Dioxide suspended in Kerosene and Linseed oil are presented in Fig. 6. The images elucidate the impact of taper on the laminar separation bubble and fluid flow behavior. Results are presented for three  $\lambda$ 's and  $\alpha$ 's at  $Re = 100,000$  and  $150,000$ . In the attached flow regime ( $\alpha = 5$  deg) the primary effect of  $Re$  is to shorten the bubble, but not the initial location of separation, a result consistent with other studies [14]. For  $\lambda = 0.4$  and  $1$ ,  $Re$  does not have a notable impact at  $\alpha = 10$  or  $14$  deg. For  $\lambda = 0.2$ , the extent of separation at  $Re = 100,000$  is greater than at  $150,000$ , in accordance with the data in Fig. 5c where the difference in  $C_{L,max}$  for  $\lambda = 0.2$  is far greater between  $Re = 100,000$  and  $150,000$  than for the other taper ratios. At  $\alpha = 5$  and  $10$  deg, a laminar transitional bubble is present for all geometries and  $Re$ .

In the predominately attached flow regime ( $\alpha = 5$  deg), the bubble extent appears to scale linearly towards the tip, but not proportionally to the taper. The bubble reduces in physical extent



**Fig. 9** Effect of viscosity on spanwise lift coefficient distribution estimated using nonlinear numerical lifting line theory.

(actual length) but occupies a greater portion of the local chord, see Table 1. As seen, the chordwise extent occupied by the bubble increases towards the wing tip as  $\lambda$  drops. The bubble terminates inboard of the wing tip due to the influence of the wing tip vortex. For both  $Re$ , the length of the bubble inboard is relatively invariant at approximately 20% of the local chord, Table 1. In the tip region, the location of separation marking the forward extent of the bubble moves progressively forward as  $\lambda$  reduces. The increase in local  $C_l$  and forward movement of the suction peak as the wing tip is approached enhances the adverse pressure gradient promoting separation.

At  $\alpha = 10$  deg, the bubble moves closer to the leading edge for all geometries due to a forward migration and enhancement of the suction peak. For the tapered wings, turbulent separation manifests in the formation of a line of separation near the trailing edge precipitated by spanwise flow from the wing tip to the root. The magnitude of the spanwise flow (interpreted as curvature of the skin friction lines) is enhanced as  $\lambda$  reduces. This implies greater spanwise pressure gradients in the trailing-edge region. Clearly visible are skin friction lines originating at the bubble and streaming aft to coalesce into the aft line of separation implying that the bubble is not continuously bounded by a closed separation stream surface. These skin friction lines were observed to originate during periodic “venting” of the laminar bubble where fluid was ejected aft. At  $\alpha = 14$  deg, all geometries show large extents of flow separation consistent with stall

(Figs. 5a and 5b). The extents of separation are seen to be moderately larger at  $Re = 100,000$  than 150,000 for  $\lambda = 0.4$  and 1. This is not the case for  $\lambda = 0.2$  where massive separation is visible at  $Re = 100,000$ , while at  $Re = 150,000$  a region of attached flow is evident inboard and ahead of the line of separation. For all cases, the aft spanwise separation line is seen to terminate in a focus of separation near the trailing edge at the root. At  $\alpha = 14$  deg, a focus of separation was visible near the wing tip for  $\lambda = 0.2$  (with rotation clearly evident in video recorded during testing). Examination of the video material also showed that for this geometry, the flow was unstable at high incidence, with periodic fluidic eruptions and oscillations in the wing tip focus which coupled with unsteadiness in the large scale inboard separation.

The effect of finite span on the bubble behavior was examined through additional sectional testing. The wing ( $\lambda = 1$ ) was extended to the tunnel walls using an extension piece yielding sectional characteristics. Tests were conducted such that the  $Re$  matched that of the  $\lambda = 0.2$  wing at the midspan (local  $Re$  number of 150,000) and 0.9 of the span (local  $Re$  of 90,000) at  $\alpha = 5$  deg. The lift coefficient of the wing and airfoil section were also matched. Results are summarized in Table 2 with presentation in Fig. 6. The chordwise extent (length) of the bubble appears little affected by three dimensionality. At the midsemi-span location, the bubble characteristics are similar to those of the airfoil at the same  $Re$ . However finite wing effects manifest in the tip region, where the bubble is located further

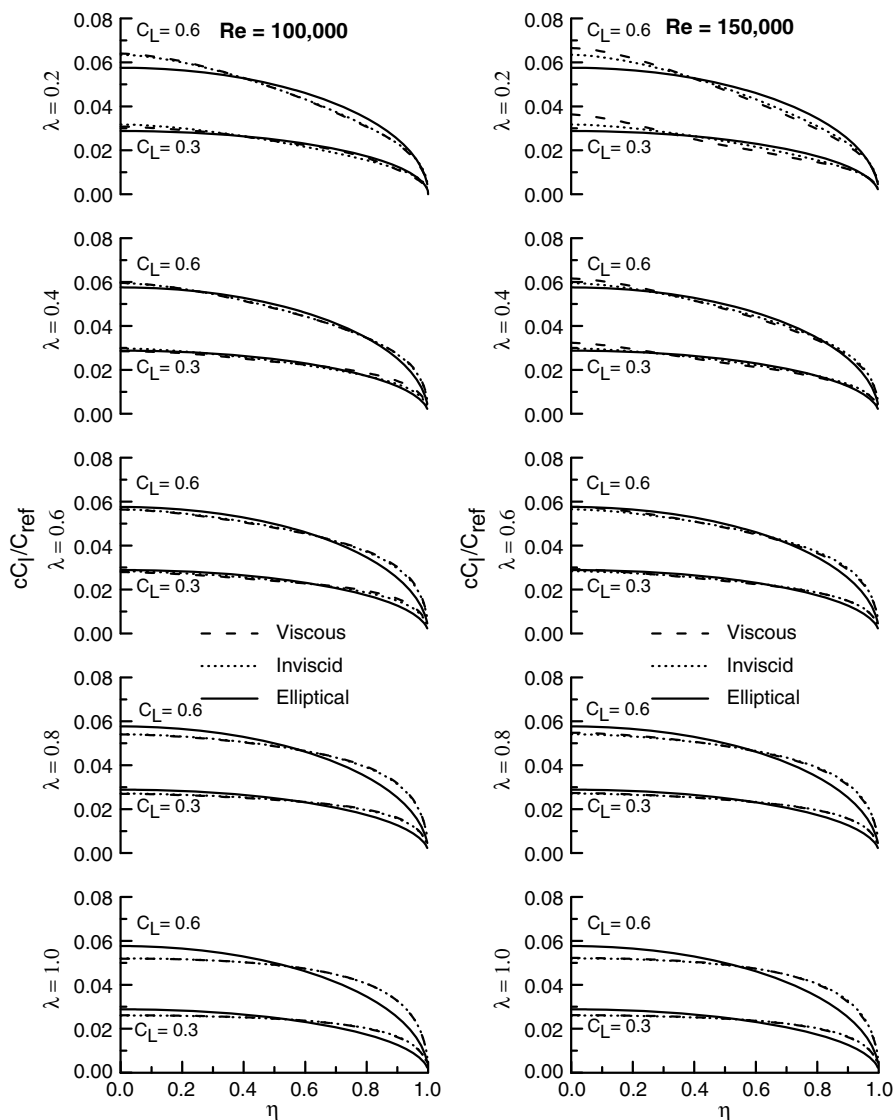


Fig. 10 Effect of viscosity on spanwise load distribution estimated using nonlinear numerical lifting line theory.

forward than on the airfoil at the same  $Re$ . This follows from the tip being at a higher loading condition (local  $C_l$ ) than the airfoil.

### Comparison of Theory and Experiment

Figure 7 shows a  $C_L$  comparison of the nonlinear lifting line theory with experiment for both  $Re$ . The predictions are seen to show good agreement with experiment. Nonlinearities in the lift curve associated with bubble motion and displacement thickness effects [15,16] are well captured. Predictions cannot be made into the stall region as  $\alpha_{zL}$  tends to negative infinity as the lift curve plateaus.

Figure 8a and 8b present estimates of the drag coefficient predicted using the nonlinear lifting line code and analytic theory [Eqs. (2) and (9)]. The analytic approach calculates the sectional pressure drag estimate based upon the airfoil data collected at the  $Re$  of the mean chord of the tapered wing. The close accord shown in Figs. 8a and 8b between experiment and both theoretical approaches is encouraging and supports the simplification in the estimate of the sectional pressure drag in the analytic approach. The estimate of the minimum drag coefficient is similar for both theoretical approaches and in accord with experiment. The lift dependent drag, which reflects in the curvature of the polar is well approximated by both methods. The drag due to lift comprises both sectional pressure drag and inviscid vortex drag. The premise of estimating the wing's profile pressure drag based upon airfoil characteristics at the mean  $Re$  for the wing is seen to improve with Reynolds number in the  $Re$  range explored (the

theoretical predictions in Fig. 8b are indistinguishable). This follows as an increase in freestream  $Re$  yields a smaller variation in the spanwise drag coefficient as the  $C_d$  variation with Reynolds number lessens as  $Re$  increases, see Fig. 4.

Figure 8c and 8d examine the lift dependent drag characteristics explicitly as affected by  $Re$ . Also included is the inviscid result, which represents full leading-edge suction for the geometry (i.e., not for elliptic loading). Immediately apparent is the magnitude of the sectional pressure drag contribution to the total lift dependent drag. Also observed is a reduction in this drag component as  $Re$  is increased from 100,000 to 150,000 interpreted as the difference between the experimental data and the "Inviscid Solution" line. Increasing taper shows a systematic reduction in sectional pressure drag for both  $Re$  (i.e., the gap between the experimental data and the inviscid solution line reduces). This implies that the benefit of increased chord and thus inboard  $Re$  tends to outweigh the chord and  $Re$  reduction towards the wing tips.

Figures 9–12 show spanwise lift and drag distributions illuminating the effect of viscosity as predicted using the numerical lifting line formulation. Figure 9 implies that viscous effects have a negligible effect on the spanwise local lift coefficient for taper ratios above 0.6. Below  $\lambda = 0.6$  viscosity (through alteration of the local lift curve in terms of slope and extrapolated  $\alpha_{zL}$ ) alters the spanwise  $C_l$ 's with an apparent dependence on  $Re$ . For reference, the spanwise load distribution (Fig. 10) also includes a curve representing elliptic spanwise loading. Familiar trends associated with taper are evident,

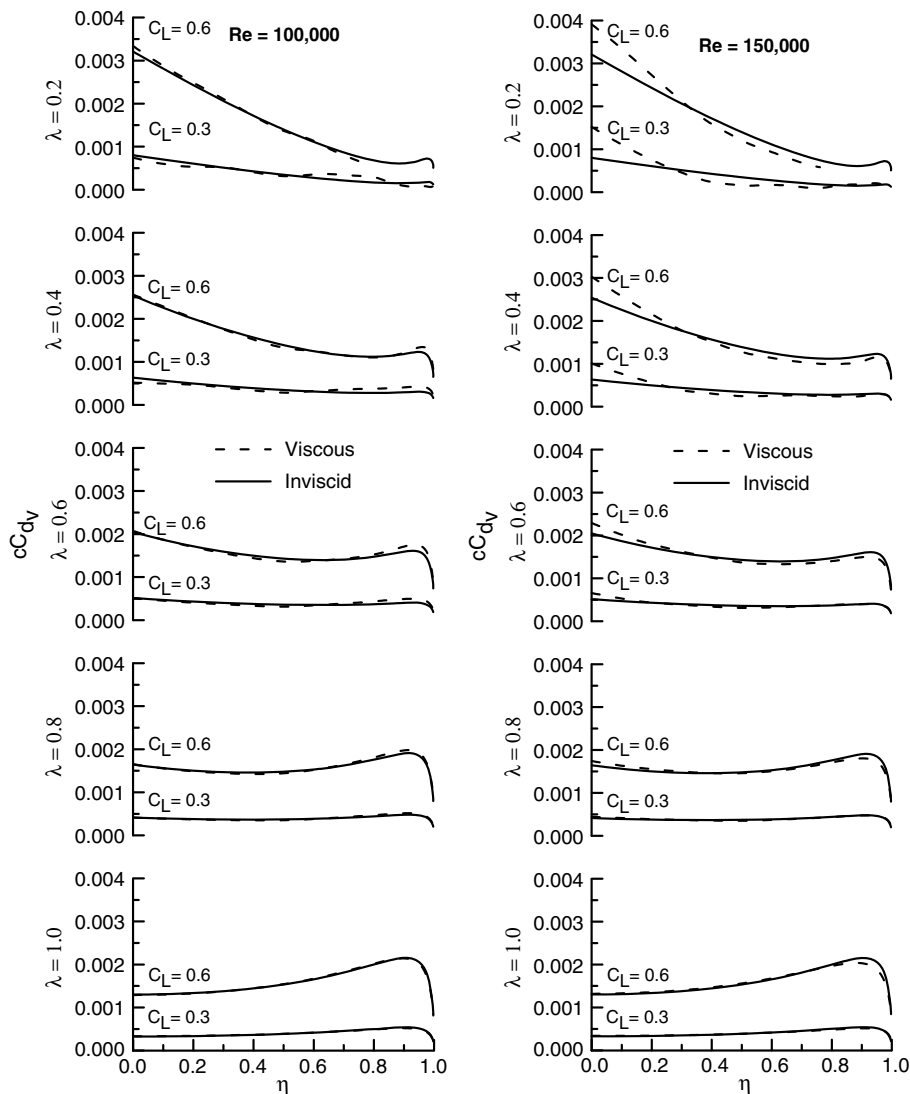


Fig. 11 Effect of viscosity on spanwise induced drag distribution estimated using nonlinear numerical lifting line theory.

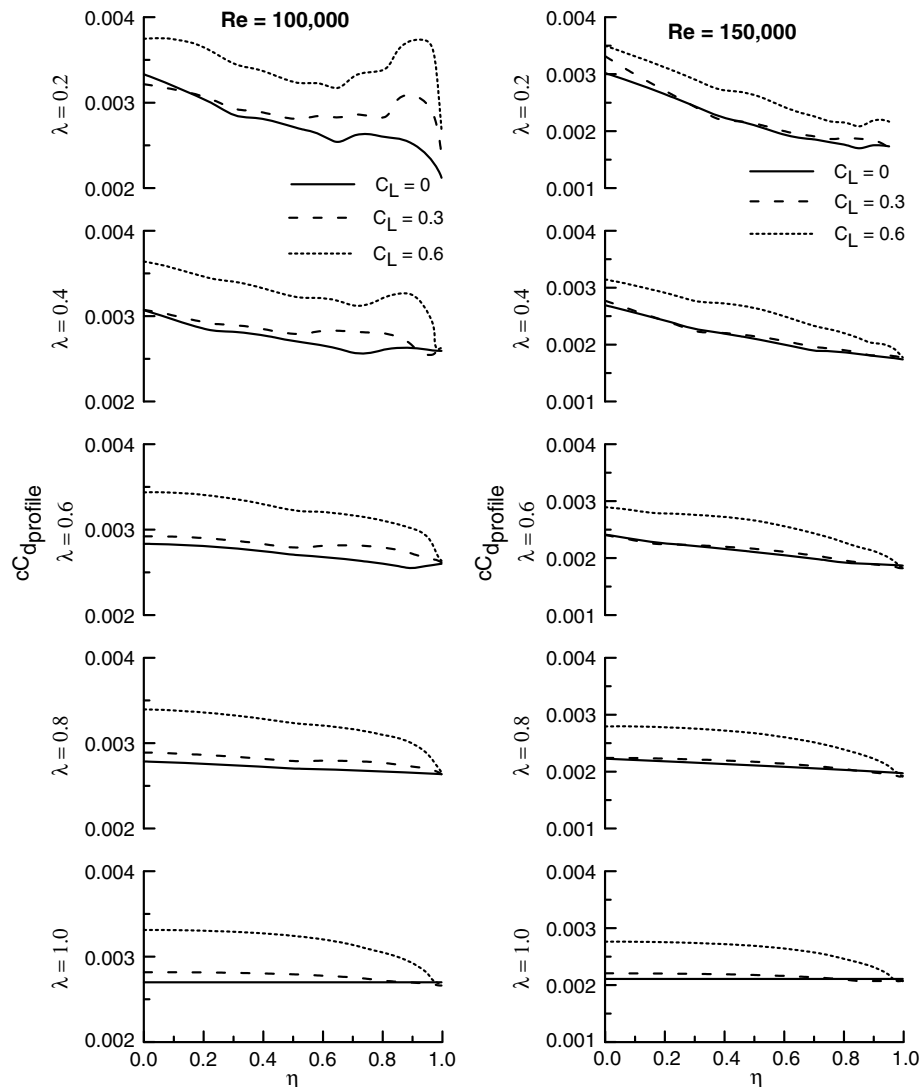


Fig. 12 Effect of viscosity on spanwise profile drag coefficient distribution estimated using nonlinear numerical lifting line theory.

where low taper ( $\lambda$  close to 1) increases loading outboard,  $\lambda = 0.4$  approximates elliptic loading (consequently yielding an  $e_i$  just below 1 [4]) and high taper ( $\lambda$  close to 0) increases loading inboard and attenuates it outboard. Viscosity is seen to only have a significant effect for high taper ( $\lambda = 0.2$ ) and  $Re = 150,000$ . For this case viscosity increases loading inboard and reduces it outboard compared to the inviscid case.

The spanwise variation of the vortex drag is presented in Fig. 11. The alterations to the spanload distribution changes the trailing vorticity strength yielding variation in the distribution of the inviscid drag. Consequently, the vortex drag is increased inboard and reduced over the midsection of the wing most notably for  $Re = 150,000$  and  $\lambda = 0.2$  and  $0.4$ . Taper is seen to shift the balance of the vortex drag; low taper (high  $\lambda$ ) yielding most vortex drag generation near the wing tip while high taper causes significant vortex drag production near the wing root. Figure 12 shows the spanwise profile drag distribution, which comprises both the skin friction and sectional pressure drag. The profile drag is generated primarily in the inboard regions, with this behavior strengthening as the taper ratio increases (lower  $\lambda$ ). This follows from the greater extent of chord inboard overpowering the drop in the local sectional drag coefficient. At lower  $Re$ , the nonlinear increase in the drag coefficient outboard (see Fig. 1) yields a significant increase in sectional profile drag outboard despite the reduction in the local chord.

Coupling of the numerical lifting line theory with an optimizer as described prior allows development of planform shapes that mini-

mize the total drag coefficient. Figure 13 shows planform examples for two aspect ratio and  $Re$  numbers at  $C_L$  of 0.3. Airfoil characteristics were established using the current experimental data as well as Xfoil simulation. Optimization tends to drive up the wing tip chord compared to an elliptic planform so as to minimize the drag penalty in the tip regions (due to the low  $Re$ ). Sensitivity to the prediction of the airfoil characteristics is evident. Xfoil generally under predicts the drag coefficient compared to experiment [14]. This causes optimization to lessen the tip chord so as to reduce the inviscid (vortex) drag. Experimental data, which indicate higher sectional drag coefficients tends to increase the tip chord such that the increase in vortex drag (as  $\lambda \rightarrow 1$ ) is outweighed by the profile drag reduction. These results suggest that at low  $Re$  in the AR range of this study the use of an airfoil section with high profile drag will yield a pseudo-rectangular planform as optimal.

## Conclusions

A low speed experimental investigation is presented quantifying the effect of taper ratio at low  $Re$ . Characterization of the airfoil behavior was followed by wind-tunnel testing of AR = 5.56 wings with taper ratios ranging from 0.2 to 1. Test conditions encompassed  $Re = 100,000$  and  $150,000$ . The wind-tunnel data did not show any decisive trends as to an optimal taper ratio to achieve best performance. Two theoretical methods, one analytic and the other an extended nonlinear viscous lifting line theory are presented. Both

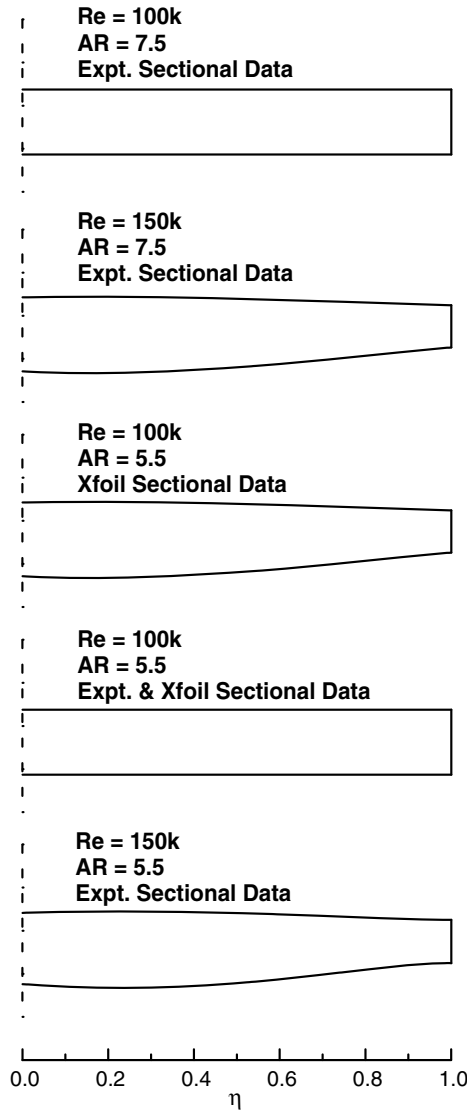


Fig. 13 Optimized planform shapes.

methods showed good agreement with experiment for estimates of the total wing drag coefficient, while the numerical lifting line method also showed good agreement in estimation of the nonlinear lift curve slope common at low  $Re$ . Coupling of the numerical method

with an optimizer suggested a sensitivity to airfoil efficiency in determination of an optimal planform. Greater airfoil drag rise would drive the solution to a rectangular planform. Higher airfoil efficiency would yield planforms of pseudo-straight taper.

References

[1] Prandtl, L., and Tietjens, O. G., *Applied Hydro and Aeromechanics*, Dover Books, New York, 1957, pp. 185–209.  
 [2] Prandtl, L., “Theory of Lifting Surfaces,” NACA TN-9, July 1920.  
 [3] Smith, S. C., and Kroo, I., “Computation of Induced Drag for Elliptical and Crescent-Shaped Wings,” *AIAA Journal*, Vol. 30, No. 4, 1993, pp. 446–452. doi:10.2514/3.46365  
 [4] McCormick, B. W., *Aerodynamics, Aeronautics, and Flight Mechanics*, 2nd ed., Wiley, New York, 1995, pp. 112–118.  
 [5] Traub, L. W., “Aerodynamic Impact of Aspect Ratio at Low Reynolds Number,” *Journal of Aircraft*, Vol. 50, No. 2, 2013, pp. 626–634. doi:10.2514/1.C031980  
 [6] Shindo, S., “Simplified Tunnel Correction Method,” *Journal of Aircraft*, Vol. 32, No. 1, 1995, pp. 210–213. doi:10.2514/3.46705  
 [7] Barlow, J., Rae, W., and Pope, A., *Low-Speed Wind Tunnel Testing*, 3rd ed., Wiley, New York, 1999, pp. 367–400.  
 [8] Traub, L. W., “Analytic Drag Prediction for Cambered Wings with Partial Leading Edge Suction,” *Journal of Aircraft*, Vol. 46, No. 1, 2009, pp. 312–319. doi:10.2514/1.38558  
 [9] Anderson, J. D., *Fundamentals of Aerodynamics*, 4th ed., McGraw-Hill Higher Education, Boston, 2007, pp. 395–420.  
 [10] Bertin, J. J., *Aerodynamics for Engineers*, 5th ed., Prentice Hall, Indianapolis, IN, 2008, pp. 233–254.  
 [11] Sivells, J. C., and Neely, R. H., “Method For Calculating Wing Characteristics by Lifting-Line Theory Using Non-Linear Section Lift Data,” NACA TR-865, 1947.  
 [12] Sivells, J. C., “Experimental and Calculated Characteristics of Three Wings of NACA 64-210 and 65-210 Airfoil Sections,” NACA TN-1422, 1947.  
 [13] MathWorks, *MATLAB Optimization Toolbox User’s Guide*, MathWorks, Natick, MA, 2013.  
 [14] Traub, L. W., and Cooper, E., “Experimental Investigation of Pressure Measurement and Airfoil Characteristics at Low Reynolds Numbers,” *Journal of Aircraft*, Vol. 45, No. 4, 2008, pp. 1322–1333. doi:10.2514/1.34769  
 [15] Traub, L. W., “Effect of Rapid-Prototyped Airfoil Finish on Loading at Low Reynolds Numbers,” *Journal of Aircraft*, Vol. 50, No. 1, 2013, pp. 307–311. doi:10.2514/1.C031811  
 [16] Traub, L. W., “Experimental Investigation of the Effect of Trip Strips at Low Reynolds Number,” *Journal of Aircraft*, Vol. 48, No. 5, 2011, pp. 1776–1784. doi:10.2514/1.C031375